The Astrophysical Journal, 861:81 (7pp), 2018 July 10 https://doi.org/10.3847/1538-4357/aac821

The Stellar Halo of the Spiral Galaxy NGC 1560

Laura Greggio[1], Renato Falomo[1], and Riccardo Scarpa[2,3]
[1] INAF, Osservatorio Astronomico di Padova, Vicolo dell'Osservatorio 5 I-35122 Padova, Italy; laura.greggio@oapd.inaf.it
[2] Instituto de Astrofisica de Canarias, C/O Via Lactea, s/n E38205, La Laguna (Tenerife), Spain
[3] Universidad de La Laguna, Dpto. Astrofsica, s/n E-38206 La Laguna (Tenerife), Spain
Received 2018 March 23; revised 2018 May 15; accepted 2018 May 23; published 2018 July 6

Abstract

We report on the detection of a stellar halo around NGC 1560, a $10^9\,M_\odot$ spiral galaxy member of the Maffei group. We obtained deep images in the *r*- and *i*-bands using the 10.4 m Gran Telescopio Canarias in a field centered at ∼3.7 arcmin (projected distance of 3.5 kpc) from the center of this galaxy. The luminosity function and the color–magnitude diagram show a clear excess of stars with respect to the expected foreground level at magnitudes fainter than the red giant branch tip at the distance of NGC 1560. The colors of the halo stars imply a metallicity of $Z \sim Z_\odot/50$, while their counts correspond to a stellar mass of $\sim 10^7\,M_\odot$ in the sampled region. Assuming a power-law profile for the surface mass density of the halo, our data suggest a total stellar mass of $10^8\,M_\odot$ for the halo of NGC 1560.

Key words: galaxies: halos – galaxies: individual (NGC 1560) – galaxies: structure

1. Introduction

According to models of galaxy formation in a hierarchical universe, the accretion and disruption of low-mass satellite galaxies that get captured in the potential well of the main host result in the build-up of extended stellar halos around galaxies (e.g., Cooper et al. 2010). This scenario is strongly supported by the detection of structures in galaxy halos (e.g., Ferguson et al. 2002), including signatures of ongoing accretion taking place (Foster et al. 2014; Martínez-Delgado et al. 2015). Structures in galaxy halos are usually detected in integrated light (Martínez-Delgado et al. 2010; Miskolczi et al. 2011; Merritt et al. 2016), but only if their surface brightness is high enough. However, the accreted units are eventually completely dissolved, their stars making up a smooth, diffuse, low-surface-brightness stellar halo. For such components, star counts are more effective to detect and measure the properties (mass, age, and metallicity) of the stellar halos, which show up as an excess of sources above the general background. Adopting this technique, several studies have mapped the smooth stellar halos around galaxies (Mouhcine et al. 2005, 2010; Barker et al. 2009; Tanaka et al. 2011; Greggio et al. 2014; Harmsen et al. 2017). These studies mostly pertain to galaxies with masses comparable to the Milky Way, or more massive, a range in which the potential well of the host galaxy is deep, making the accretion of several units well justified.

At the other mass end, extended stellar halos have also been revealed in many dwarf galaxies (see, e.g., Minniti & Zijlstra 1996; Stinson et al. 2009; McConnachie 2016). In some cases, the merging of two dwarf galaxies takes place, as clearly documented for NGC 4449 (Martínez-Delgado et al. 2012; Rich et al. 2012), making low-mass units eventually provide a stellar halo to the more massive accretor (Bekki 2008). However, this occurrence could be rare in the standard picture of hierarchical structure formation, and other mechanisms have been proposed to be responsible for the extended halo of dwarfs. In particular, hydrodynamical simulations of galaxy formation show that extended halos might form around dwarf isolated galaxies due to the contraction of the star-forming envelope, and the ejection of stars formed in supernova-driven shocks. The latter process is particularly effective in the lower-mass models, with the shallower potential well providing a weaker barrier to the supernova-driven outflows (Stinson et al. 2009).

In this scenario, low-mass spiral galaxies could be at the crossroads of these two paths of stellar halo formation. Massive enough to inhibit a pronounced dispersion of their stars due to the supernova-driven outflows, but not massive enough to efficiently accrete smaller units, these galaxies could host the least conspicuous stellar halos, either in mass fraction, or extension, or both. Thus, we can derive important clues regarding the general picture of formation of stellar halos by investigating this class of galaxies with the following questions in mind. Do low-mass spirals host stellar halos? What is their mass, extension, and density profile? Do they resemble a scaled-down version of the halos of more massive spirals?

The most effective way to measure the properties of a diffuse, low-surface-brightness stellar halo is via individual star counts. In stellar populations older than ∼2 Gyr the evolved stars gather on the red giant branch (RGB), forming a recognizable feature on the color–magnitude diagram (CMD). The number of stars per unit mass of the parent stellar population on the upper magnitude of the RGB is almost independent of age from ∼2 to ∼10 Gyr (e.g., Greggio & Renzini 2011), making these stars effective and robust probes of the total underlying stellar mass.

In this paper we present *i*- and *r*-band photometry of stars in a field located in the halo of NGC 1560 (Section 2), based on observations at the Gran Telescopio CANARIAS. The program aimed primarily to assess whether NGC 1560 hosts a stellar halo, and, if it did, to estimate its size. In Section 3 we describe the observations and the data reduction procedure; in Section 4 we present the CMD and luminosity function of the stars in the NGC 1560 halo field; and in Section 5 we summarize our results and discuss them in comparison to the properties of other galaxies and to the predictions of galaxy formation models.

2. The Low-mass Spiral Galaxy NGC 1560

NGC 1560 is a late-type spiral galaxy (Scd, Sdm) member of the Maffei Group. The distance (3.27 Mpc) to NGC 1560 was evaluated by Jacobs et al. (2009) from the location of the tip of

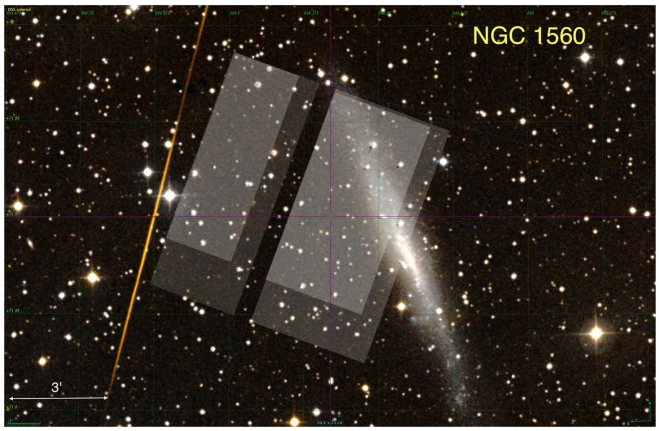

Figure 1. Field observed at GTC superposed onto a color image of the galaxy NGC 1560 from the Digitized Sky Survey. The gray areas represent the final field observed in the *i*- and *r*-bands (light gray). The final usable field of view results from the combination of several individual images with a dithering pattern. In the case of the *r*-band the field is smaller (see the text). The field of view of the DSS image is ~19.5 × 13 arcmin^2. North is up and east is to the left. The scale of 3 arcmin corresponds to a linear scale of 2.9 kpc at the distance of NGC 1560.

the RGB on the CMD derived from *HST* photometry in *V* and *I*. The object is located at low galactic latitude ($b = 16°$), making the foreground extinction quite large ($E(B-V) \simeq 0.18$). This galaxy is relatively isolated: the two nearest companions are Cam A and Cam B at distances of ~500 and ~400 kpc, respectively (Karachentsev et al. 2004).

The stellar disk is viewed edge-on (inclination of ~80°), and it is embedded in an extended H I disk, characterized by regular contours. From the analysis of the H I rotation curve, Gentile et al. (2010) derived a total (dark + luminous) mass of $\sim 4 \times 10^{10} M_\odot$, and they estimated a stellar mass of $\sim 5 \times 10^{8} M_\odot$ from *I*-band photometry. Therefore, NGC 1560 is a very good candidate to investigate the properties of stellar halos at the low-mass end of spiral galaxies, and it has a favorable edge-on orientation that allows an unambiguous sampling of the halo component.

On the Padova isochrones[4] (Marigo et al. 2008) the RGB tip of a 10 Gyr old stellar population is found at $M_i \simeq -3.25$ and −3.47, respectively, for metallicities $Z = 0.004$ and 0.0004. The foreground galactic extinction is of 0.32 and 0.43 mag in the *i* and *r*-bands, respectively. Correspondingly, we expect the RGB tip of an old and metal-poor stellar population in the halo of NGC 1560 to be found at $i \sim 24.5$. In the following we will adopt this reference value to flag the presence of RGB stars members of NGC 1560.

3. Observations, Data Reduction, and Analysis

We imaged one field centered at a distance of 3.7 arcmin from the center of the dwarf spiral galaxy NGC 1560 in order to investigate its halo stars (see Figure 1). The observations were obtained using the imager OSIRIS[5] (Cepa et al. 2003) at the Gran Telescopio CANARIAS (GTC) in La Palma. The imager includes two CCD detectors separated by a small gap, allowing a total usable field of 7 × 8 arcmin^2. We secured several short exposure images of both fields using the Sloan filters *r* and *i* with individual exposure times of 60 s. In order to improve the quality of the final images, the pointing was changed with a pattern of ~5–10 arcsec. In the case of the observations in filter *r,* two slightly different pointings where adopted, resulting in a smaller final field of view with respect to that obtained in filter *i* when combining all frames (see Figure 1). All the images were reduced using IRAF,[6] including bias subtraction, flat-field correction, and cleaning of cosmic rays and other minor defects in the detectors. Using the measured positions of a number of relatively bright, unsaturated, and isolated stars in the frames, the images were then realigned and co-added. The parameters of the final images are reported in Table 1. The quality of the final images is good, resulting in a PSF with a FWHM of 0.85 arcsec in both filters. Finally, we used observations of photometric standard stars to perform the absolute photometric calibration of the frames.

The final observed field is shown in Figure 1, superimposed on a SDSS image of NGC 1560, while Figure 2 shows the co-added *i*-band images of the two chips of the OSIRIS detector.

Table 1
Properties of the Observed Fields of NGC 1560

Field	Filter	FoV (arcmin)	N. of Frames	Tot. Exptime (s)
1	*i*	2.8 × 7.7	90	5850
2	*i*	3.8 × 7.7	90	5850
1	*r*	2.1 × 6.2	88	5720
2	*r*	3.2 × 6.2	88	5720

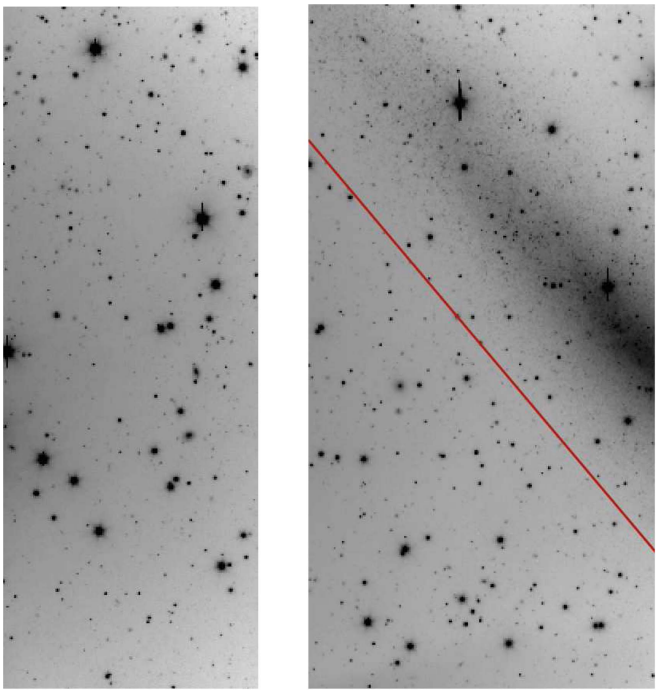

Figure 2. Image in filter *i* of chip 1 (left) and chip 2 (right panel), observed at GTC close to the galaxy NGC 1560. The total exposure time of filter *i* is 1.6 hr. The red line on chip 2 limits the region (lower part of the image) considered for the analysis, which is referred to as chip 2a in the text.

[4] stev.oapd.inaf.it/cgi-bin/cmd.
[5] http://www.gtc.iac.es/instruments/osiris/osiris.php.
[6] IRAF (Image Reduction and Analysis Facility).

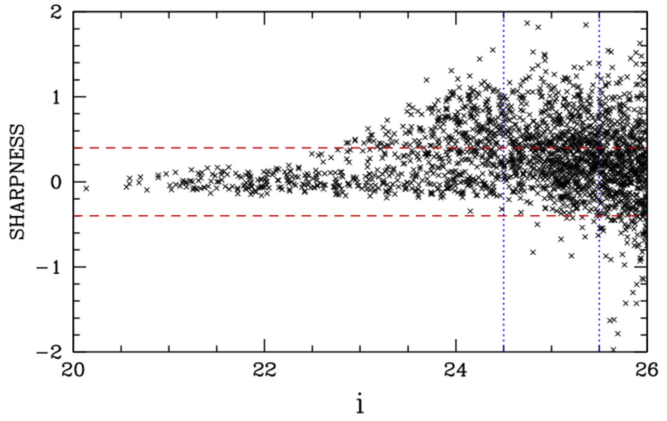

Figure 3. Sharpness parameter as a function of magnitude for the sources detected in the *i*-band in chip 1 and in chip 2a. The red dashed lines show our criteria adopted to select bona fide stars. The dotted vertical lines show the magnitude range used to map the members of NGC 1560, i.e., the upper magnitude on the RGB.

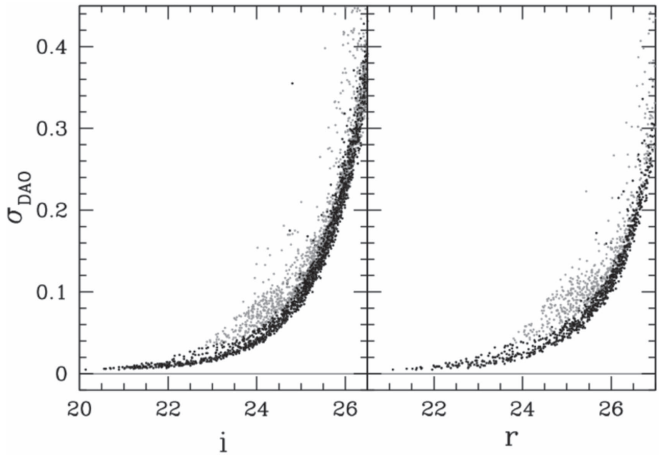

Figure 4. Photometric error parameter from DAOPHOT ($\sigma_{\rm DAO}$) as a function of magnitude in the *i*- (left) and *r*-bands (right). The plots show the combination of detections on chip 1 and on chip 2a. The black points highlight sources with sharpness between −0.4 and 0.4.

3.1. Stellar Photometry

We performed PSF photometry on the co-added images using the DAOPHOT suite of programs. PSF photometry allowed us to characterize the shape of the sources, allowing us to separate stellar from extended objects. Magnitudes were measured with the ALLSTAR routine fitting a PSF constructed with the DAOPSF task, using a number of bright and isolated sources on the individual chips. With a detection threshold of 2.5σ, on the *i*-band images we measured 2180 sources on chip 1 and 8837 on chip 2, down to $i \simeq 27$. In the *r*-band images we measured 1195 and 5435 sources down to $r \simeq 27.5$ on chip 1 and chip 2, respectively. Chip 2 includes a portion of the disk of NGC 1560, where crowding is high. Since we concentrate on the halo population, in our analysis we only consider sources detected at a distance greater than 1.3 arcmin (corresponding to ∼1.2 kpc) from the plane of the disk (see Figure 2), where we count 1619 and 565 sources in the *i* and *r* frames, respectively. Hereafter, this portion of chip 2 will be referred to as chip 2a.

We complement our photometric analysis with artificial stars experiments, in which we add a number of artificial stars with magnitudes in the range 24.5–26.7 to the *i*-band image. We then perform photometry of the frame including the artificial stars, adopting the same DAOPHOT parameters as used on the original image. These experiments allowed us to refine the criteria to select stellar objects from the quality parameters of the DAOPHOT package (χ^2 and sharpness), as well as to assess the error (as the difference between the input and output magnitudes) and the completeness of detected stars as a function of their magnitude.

Based on the distribution of the χ^2 parameter, we discarded the objects with $\chi^2 \geqslant 0.5$. This criterion excludes ∼10% of the sources; most of them are bright, saturated foreground stars. Figure 3 shows the distribution of the sharpness parameter as a function of the magnitude of the sources, for objects brighter than $i = 26$, that is ∼1.5 mag fainter than the expected location of the RGB tip. At $i \lesssim 24$, most of the sources have a sharpness between −0.2 and 0.2, but at fainter magnitudes the spread grows. At $i \gtrsim 24$, a large number of sources with high and positive sharpness values appear. Guided by the results of the artificial stars experiments, we selected as bona fide stars the sources with sharpness smaller than 0.4. Upon visual inspection, most sources with sharpness higher than this appear as extended objects. The lower limit to the sharpness parameter adopted is −0.4. The total numbers of bona fide stars are 983 and 789, respectively, on chip 1 and on chip 2a. The distributions of the χ^2 and sharpness parameters on the *r*-band images have very similar characteristics as those of the *i*-band images. There are 539 bona fide stars in chip 1 and 340 in chip 2a.

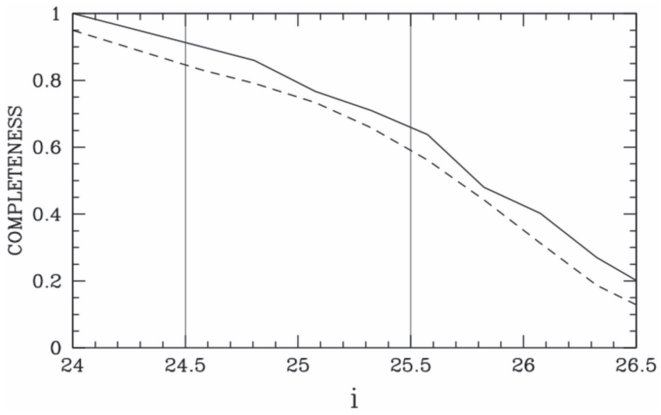

Figure 5. Fraction of artificial stars recovered and measured with sharpness between −0.4 and +0.4 as a function of input magnitude on chip 1 (solid) and chip 2a (dashed). The vertical lines show the magnitude of the RGB tip and one magnitude fainter than this. These levels limit the region used to estimate the stellar mass from the star counts.

Figure 4 shows the DAOPHOT photometric accuracy parameter ($\sigma_{\rm DAO}$) as a function of magnitude for the *i*- and *r*-bands in the two chips, having again excluded the disk of NGC 1560. The adopted criteria to select the bona fide stars also selects for the best measured objects.

We use the results of the artificial stars experiments to evaluate the completeness of our data as a function of magnitude by comparing the number of stars measured on the images with the synthetic stars added, to the number of input artificial stars. Figure 5 shows the completeness factors as a function of the magnitude. We note that in the magnitude range of interest the completeness of our data is better than 50% for the bona fide selected sources. The artificial stars experiments were also used to evaluate the true error on the

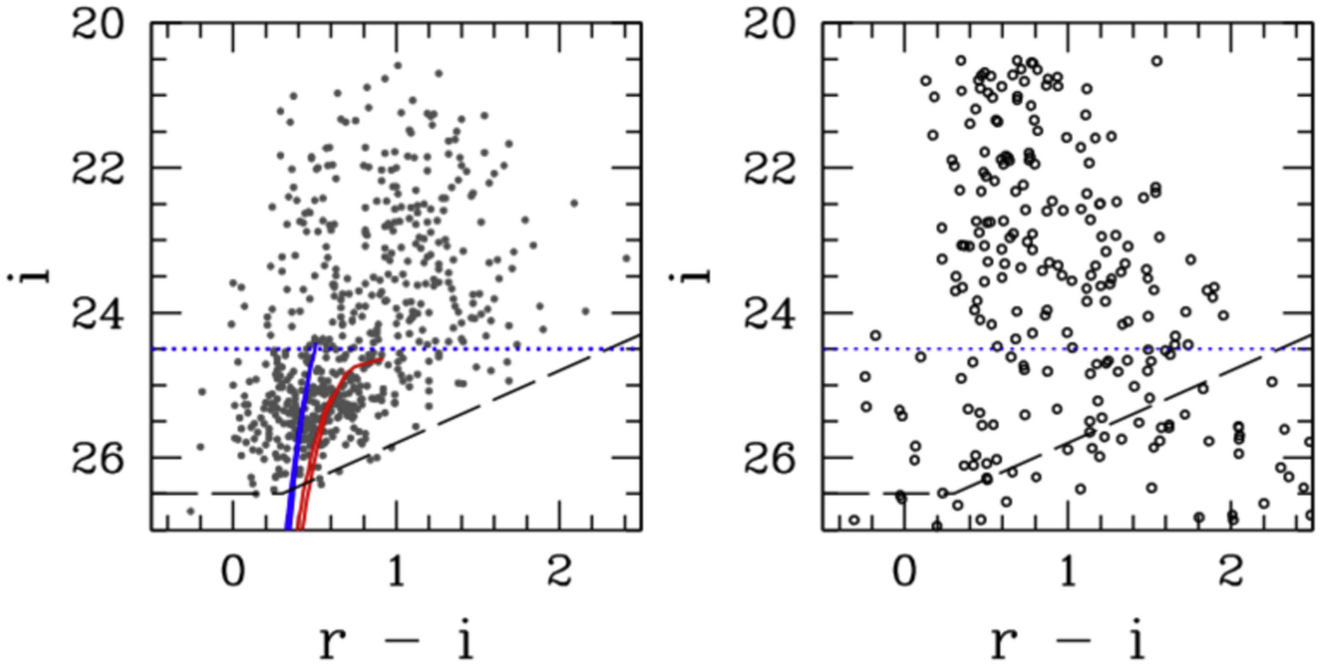

Figure 6. Left: CMD of the bona fide stars measured on chip 1 and on chip 2a (gray points). The solid lines show 10 Gyr old Padova isochrones for metallicity $Z = 0.0004$ (blue) and $Z = 0.004$ (red) at the distance of NGC 1560, including the foreground galactic reddening. Right: CMD of a simulation of the foreground stars in the direction of NGC 1560 for an area close to the surveyed area (see the text). Objects brighter than $i = 20.5$ are not plotted on this CMD, as they do not appear on the observed CMD due to saturation. In both panels the dotted line shows the level of the RGB tip, and the dashed line shows the magnitude limits of our observations ($i = 26.5$, $r = 26.8$).

measured magnitude of the bona fide stars. Down to $i \sim 26$, the distribution of $\Delta m = m_{\rm output} - m_{\rm input}$ is found to be symmetric around 0, with a dispersion of 0.1, 0.15, and 0.2 for $i \simeq 25$, 25.5, and 26 respectively. At fainter magnitudes the distribution becomes noticeably skewed toward negative values of Δm because sources artificially brightened by blending are more likely to be detected than sources whose brightness is underestimated (see Greggio & Renzini 2011). We conclude that in the range $i \lesssim 26$, the quality of our photometry is satisfactory.

4. The Stellar Halo around NGC 1560

Matching the sources detected in both the *r*- and *i*-bands, we get 302 and 284 bona fide stars, respectively, on chip 1 and on chip 2a. Figure 6 shows the relative CMD, to which we superpose 10 Gyr old Padova isochrones with two subsolar metallicities. We compare this CMD with the result of a simulation of the foreground contamination obtained using the TRILEGAL[7] tool (Girardi et al. 2005), at the galactic coordinates of NGC 1560 (see Figure 6, right panel). The simulation is computed for an area of 25 arcmin^2, close to the area on which our observed CMD is constructed. At magnitudes brighter than our fiducial RGB tip, the observed CMD is very similar to the simulated one, but fainter than the RGB Tip there is a clear excess of observed stars with colors appropriate to those for a metal-poor old stellar population. The expected number of foreground stars at $i > 24.5$ is significantly smaller than that observed. In addition, at these magnitudes the simulated stars scatter over a much wider color range compared to the data. In the range $24.5 < i < 26$ and $0 < r - i < 1$ we count 274 stars on our CMD, while the simulation of the foreground component contains only 17 objects. We also computed a simulation of the foreground stars using the recently updated Besancon model (Robin et al. 2003),[8] which yields 12 expected foreground objects in this region of the CMD, i.e., even less than the TRILEGAL simulation. This indicates that the observed CMD contains a population of member stars of NGC 1560. In the following, for the foreground stars contamination we will use the more conservative value obtained from TRILEGAL.

The star counts on the *i*-band image shown in Figure 7 further support our detection of the NGC 1560 stellar halo. Compared to the foreground, the observed star counts are close to the expected level at $i < 23$, while they show a mild excess (a factor of $\gtrsim$2) at $i \sim 24$. These excess sources could be either bright asymptotic giant branch (AGB) member stars of the NGC 1560 halo, or Milky Way stars, if the foreground contributions at these magnitudes were underestimated in the adopted Galaxy model. At $25 < i < 26$ a remarkable (a factor of $\sim$10) difference between the observed counts and the foreground level is apparent (see Figure 7). This large excess is present in both chips: the surface density of bona fide stars with $24.5 \leqslant i \leqslant 25.5$ is 11 per square arcmin in chip 1, and 16 per square arcmin in chip 2a; compare that with the 1.5 objects per square arcmin of the TRILEGAL simulation. Therefore, most of the stars fainter than $i \simeq 24.5$ belong to the stellar halo of NGC 1560.

In order to estimate the stellar mass traced by our halo field we construct a simple stellar population (SSP) model by distributing stars along an old and metal-poor isochrone, following a prescribed initial mass function (IMF). We adopt a 10 Gyr old isochrone with a metallicity of $Z = Z_{\odot}/50$ from the Padova (Marigo et al. 2008) set. The metallicity choice is motivated by the color of the RGB stars in our field (see

[7] http://stev.oapd.inaf.it/cgi-bin/trilegal.

[8] http://model2016.obs-besancon.fr/.

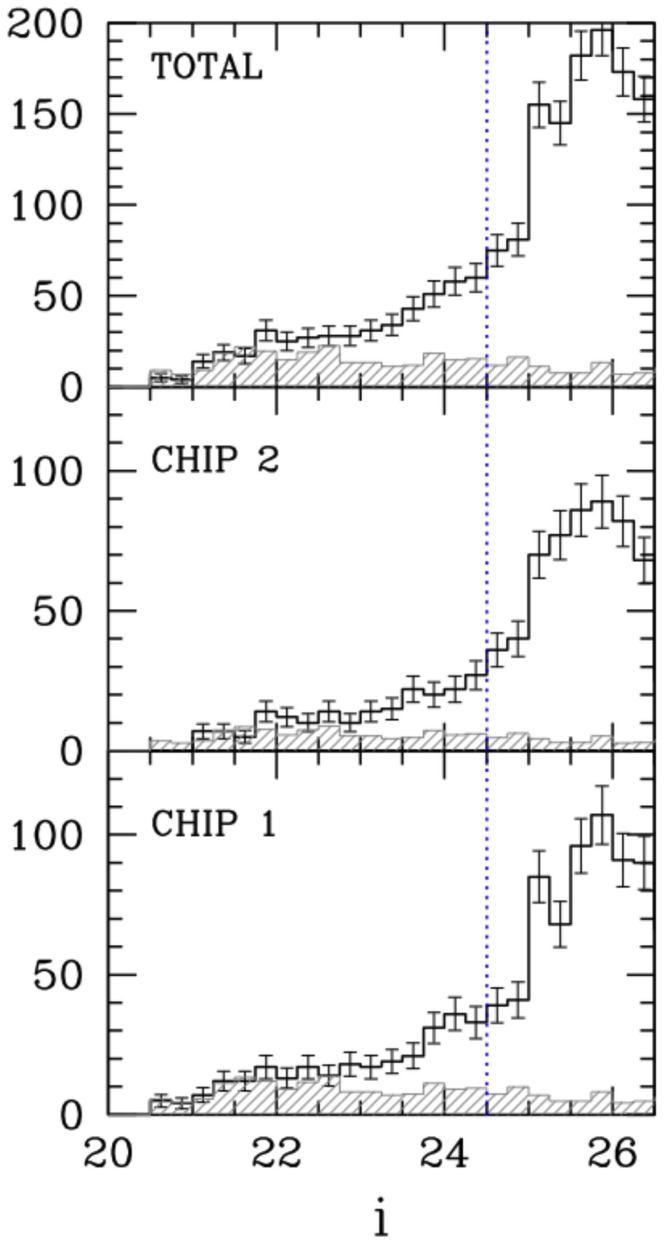

Figure 7. Magnitude distribution of the bona fide stars on the *i*-band images (unshaded histogram) compared to the TRILEGAL simulation of the foreground stars (shaded histogram). The top panel refers to the total area sampled, while the central and bottom panels refer to the individual chips. The simulations are normalized to the sampled area, respectively 21.6 and 13.7 square arcmin for chip 1 and chip 2a. The vertical dotted line shows the magnitude of the RGB Tip.

Figure 6), while the adopted value of the age is not critical, since the conversion factor between bright RGB star counts and the mass of the parent stellar population is almost constant for ages older than ∼2 Gyr (Greggio & Renzini 2011). Figure 8 shows the magnitude distribution of this synthetic stellar population, compared to our data. The model is in acceptable agreement with the completeness-corrected observed counts. The normalization of the SSP model yields the total stellar mass needed to reproduce the observed star counts, which turns out to be $\sim 1.6 \times 10^7\, M_\odot$, having adopted a Salpeter IMF (between 0.1 and 100 $M_\odot$). This is the total mass transformed into stars, while the current mass will be a factor ∼0.7 lower because of the mass returned to the interstellar medium by

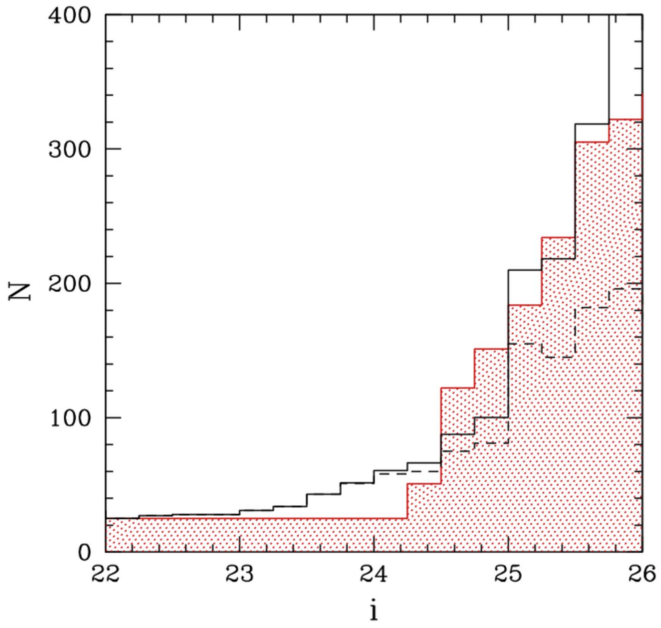

Figure 8. Magnitude distribution of the bona fide stars on the *i*-band images (unshaded black) compared to the simulation of an SSP with an age of 10 Gyr and a metallicity $Z = 0.0004$, based on the Padova tracks (shaded red). The model assumes $(m - M)_0 = 27.57$ and $A_i = 0.32$. A foreground stellar density matching the counts in $22 < i < 23$ is included in the model. The observed distribution is plotted as plain counts (dashed lines) and counts corrected for the incompleteness (solid line). Note that the expected discontinuity at the RGB tip overlaps with the components of either foreground or AGB stars at $i \sim 24$ discussed in the text.

stellar wind and supernovae over the long lifetime of the stellar population (see Greggio & Renzini 2011).

Assuming a spherical halo with a surface mass density described by a power-law index of $s = -1.5$, close to what was found for NGC 253 in Greggio et al. (2014), we find that our *i*-band image samples ∼13% of the total mass. This indicates a value of $\sim 10^8\, M_\odot$ for the stellar halo for this galaxy. Varying the power-law index, the mass fraction sampled by our field is 13% for $s \lesssim -1.5$, of 10% for $s = -2$, and decreases to ∼4% as the profile steepens to $s = -3$. Since chip 1 samples the halo in an outer region compared to chip 2, we may derive indications on the slope of the mass distribution by comparing the star counts in the two chips. The number of bona fide stars with $24.5 \leqslant i \leqslant 25.5$ is 234 in chip 1 and 223 in chip 2a. Upon correction for incompleteness, these figures respectively become 332 and 348. The counts include the halo members of NGC 1560, as well as the foreground stars, which, according to the TRILEGAL model, should amount to ∼40 stars in chip 1 and 25 stars on chip 2 in the same magnitude range. The true members of NGC 1560 should therefore be 292 and 323 in chip 1 and 2a, respectively. On the other hand, as argued above, the TRILEGAL model matches very well the star counts in the range $22 \lesssim i \lesssim 23$, but it falls short of the observed counts in $23 \lesssim i \lesssim 24.5$, where we do not expect a sizable population of NGC 1560 members. In fact, these stars should be bright AGB objects, which are very rare in stellar populations older than a few Gyr (e.g., Noël et al. 2013). If we estimate the foreground contribution from the counts at magnitudes just brighter than the RGB tip, ($i \simeq 24.3$), chip 1 and chip 2a should, respectively, include ∼120 and 76 foreground stars with $24.5 < i < 25.5$. This would leave 212 and 272 members of NGC 1560 halo stars sampled in chip 1 and 2a. From this discussion we estimate

that the ratio between the NGC 1560 halo stars in chip 1 and in chip 2a varies between 0.9 and 0.78, depending on the level of the foreground contribution to the counts. For a spherical halo with a surface mass density scaling as a power law, the ratio of mass sampled in chip 1 and chip 2a decreases from 0.7 to 0.13 as the index varies from −1 to −3. Therefore, our data suggest a quite shallow profile for the mass distribution for the halo of NGC 1560.

5. Summary and Discussion

We performed deep photometry in a region centered at a projected distance of ∼3.5 kpc from the center NGC 1560, a low-mass, late-type spiral galaxy at a distance of 3.27 Mpc. The favorable edge-on orientation of this galaxy, coupled with the relatively wide FoV of the observations, allowed us to derive a fair census of the sources projected on the halo area around NGC 1560, where we detect a large excess of stars above the expected foreground contribution. Based on the colors and magnitudes of these sources we conclude that they are bright RGB stars members of NGC 1560. Their $(r - i)$ color is appropriate for a metal-poor stellar population ([Fe/H] $\simeq -1.7$). We measure these excess sources all over the surveyed region, with no apparent concentration toward the galaxy disk. Therefore, we conclude that these stars belong to an extended stellar halo around NGC 1560.

The size of the excess counts indicates a stellar mass of $\sim 10^7\ M_\odot$ in the sampled region, assuming a Salpeter IMF. Comparing the counts in two regions of our surveyed area, we favor a quite shallow mass surface density profile of the halo component, with a slope of ~ -1 for a power-law distribution. Assuming a spherical halo with such a shallow profile, and keeping in mind the uncertainty of the foreground contribution, the sampled region collects 13% of the total halo mass, which then turns out to be $\sim 10^8\ M_\odot$.

The sampled mass and the profile that we derive depend on the assumptions regarding the contribution of the foreground stars and the background galaxies. Both the TRILEGAL and the Besancon simulators of the Milky Way population in the direction of NGC 1560 predict a negligible number of foreground sources at magnitudes fainter than the RGB tip in our sampled fields. On the other hand, the number of compact background galaxies at these faint magnitudes might be relevant. To minimize these kinds of contaminants, we have selected sources with a small value of the sharpness parameter from the DAOPHOT PSF fitting photometry. Based on the results of the artificial stars experiments, we defined as bona fide stars sources with sharpness lower than 0.4 (in absolute value). Using a more restrictive criterion, the mass sampled on chip 1 and chip 2a varies. For example, changing the threshold from 0.4 to 0.2, the number of bona fide stars decreases by ∼25% in both chips. While this corresponds to a lower mass for the stellar halo of NGC 1560, the excess of point-like sources with respect to the expected foreground stars remains significant. The detection of an extended stellar halo around NGC 1560 is thus a robust result, while the measurement of its mass and profile are subject to some uncertainty, depending on the contribution of unresolved compact galaxies.

We estimate the stellar mass of the main body of NGC 1560 from its I-band magnitude ($I = 10.26$, Buta & McCall 1999), adopting a Milky Way absorption of $A_I = 0.28$, and a mass-to-light ratio of $M/L_I = 1.7$ in solar units, which is appropriate for a stellar population with a constant star formation rate over the Hubble time, and a Salpeter IMF. With these assumptions, and our adopted distance modulus of 27.6, the mass NGC 1560 is $8 \times 10^8\ M_\odot$, making the ratio between the mass of the halo and the mass of the main body of the galaxy ∼0.1.

Harmsen et al. (2017) summarized the properties of the stellar halos of Milky Way mass spiral galaxies from the GHOSTS survey. These appear to be characterized by steep surface mass density profiles ($s \sim -2 \div -3.7$), and a large diversity of stellar halo mass fractions (∼0.01 ÷ 0.1). Our data for NGC 1560 suggest a shallower profile, and a high stellar halo mass fraction. How do these properties compare to the results of numerical simulations?

Detailed computations of the structure of galaxy stellar halos within the Λ cold dark matter cosmological model are available mostly for galaxies with masses akin to those of the Milky Way and Andromeda (e.g., Lackner et al. 2012; McCarthy et al. 2012; Cooper et al. 2013; Tissera et al. 2014). Recently, Rodriguez-Gomez et al. (2016) extended the mass range to include objects with stellar masses down to $10^9\ M_\odot$. In their models, the lowest-mass galaxies typically host an accreted stellar mass of a few percent of the total galaxy mass, but with a large variance, and an accreted mass fraction up to 0.1 is reported for galaxies of $\sim 10^9\ M_\odot$. In these models, the accreted stars are distributed in an elongated envelope characterized by a steep density drop. Steep slopes for the outer regions are also found in models of dwarf galaxies (Bekki 2008; Valcke et al. 2008; Stinson et al. 2009), and in observational data (e.g., Battinelli et al. 2006; D'Souza et al. 2014). Although a direct comparison of our results with those of other galaxies, and of theoretical models, is hindered by differences in mass and methods of analysis, it appears that in the case of NGC 1560, the stellar halo has an extended and flat profile that may pose important constraints to galaxy formation models of low-mass spiral galaxies. This halo extends over a wide region: we detect stars at distances 3× larger than the edge of the H I disk, as measured by Gentile et al. (2010). The H I distribution appears undisturbed, the galaxy is isolated, and there is no evidence of a recent interaction. This suggests that the stellar halo of NGC 1560 was acquired at an early epoch, possibly built during the original collapse that led to the formation of the disk.

The financial contribution by the contract *Studio e Simulazioni di Osservazioni (Immagini e Spettri) con MICADO per E-ELT* (DD 27/2016—Ob. Fun. 1.05.02.17) of the INAF project *Micado simulazioni casi scientifici*, P.I. Dr. Renato Falomo, is acknowledged.

This research has made use of the NASA/IPAC Extragalactic Database (NED), which is operated by the Jet Propulsion Laboratory, California Institute of Technology, under contract with the National Aeronautics and Space Administration.

Facility: GTC-OSIRIS.

ORCID iDs

Laura Greggio https://orcid.org/0000-0003-2634-4875
Renato Falomo https://orcid.org/0000-0003-4137-6541
Riccardo Scarpa https://orcid.org/0000-0001-9118-8739

References

Barker, M. K., Ferguson, A. M. N., Irwin, M., Arimoto, N., & Jablonka, P. 2009, AJ, 138, 1469
Battinelli, P., Demers, S., & Kunkel, W. E. 2006, A&A, 451, 99

Bekki, K. 2008, ApJL, 680, L29
Buta, R. J., & McCall, M. L. 1999, ApJS, 124, 33
Cepa, J., Aguiar-Gonzalez, M., Bland-Hawthorn, J., et al. 2003, Proc. SPIE, 4841, 1739
Cooper, A. P., Cole, S., Frenk, C. S., et al. 2010, MNRAS, 406, 744
Cooper, A. P., D'Souza, R., Kauffmann, G., et al. 2013, MNRAS, 434, 3348
D'Souza, R., Kauffman, G., Wang, J., & Vegetti, S. 2014, MNRAS, 443, 1433
Ferguson, A. M. N., Irwin, M. J., Ibata, R. A., Lewis, G. F., & Tanvir, N. R. 2002, AJ, 124, 1452
Foster, C., Lux, H., Romanowsky, A. J., et al. 2014, MNRAS, 442, 3544
Gentile, G., Baes, M., Famaey, B., & van Acoleyen, K. 2010, MNRAS, 406, 2493
Girardi, L., Groenewegen, M. A. T., Hatziminaoglou, E., & da Costa, L. 2005, A&A, 436, 895
Greggio, L., Rejkuba, M., Gonzalez, O. A., et al. 2014, A&A, 562, A73
Greggio, L., & Renzini, A. 2011, Stellar Populations. A User Guide from Low to High Redshift (Weinheim: Wiley)
Harmsen, B., Monachesi, A., Bell, E. F., et al. 2017, MNRAS, 466, 1491
Jacobs, B. A., Rizzi, L., Tully, R. B., et al. 2009, AJ, 138, 332
Karachentsev, I. D., Karachentseva, V. E., Huchtmeier, W. K., & Makarov, D. I. 2004, AJ, 127, 2031
Lackner, C. N., Cen, R., Ostriker, J. P., & Joung, M. R. 2012, MNRAS, 425, 641
Marigo, P., Girardi, L., Bressan, A., et al. 2008, A&A, 482, 883
Martínez-Delgado, D., D'Onghia, E., Chonis, T. S., et al. 2015, AJ, 150, 116
Martínez-Delgado, D., Gabany, R. J., Crawford, K., et al. 2010, AJ, 140, 962
Martínez-Delgado, D., Romanowsky, A. J., Gabany, R. J., et al. 2012, ApJL, 748, L24
McCarthy, I. G., Font, A. S., Crain, R. A., et al. 2012, MNRAS, 420, 2245
McConnachie, A. W. 2016, in IAU Symp. 317, The General Assembly of Galaxy Halos: Structure, Origin and Evolution, ed. A. Bragaglia et al. (Cambridge: Cambridge Univ. Press), 15
Merritt, A., van Dokkum, P., Abraham, R., & Zhang, J. 2016, ApJ, 830, 62
Minniti, D., & Zijlstra, A. A. 1996, ApJL, 467, L13
Miskolczi, A., Bomans, D. J., & Dettmar, R.-J. 2011, A&A, 536, A66
Mouhcine, M., Ibata, R., & Rejkuba, M. 2010, ApJL, 714, L12
Mouhcine, M., Rich, R. M., Ferguson, H. C., Brown, T. M., & Smith, T. E. 2005, ApJ, 633, 828
Noël, N. E. D., Greggio, L., Renzini, A., Carollo, C. M., & Maraston, C. 2013, ApJ, 772, 58
Rich, R. M., Collins, M. L. M., Black, C. M., et al. 2012, Natur, 482, 192
Robin, A. C., Reylé, C., Derrière, S., & Picaud, S. 2003, A&A, 409, 523
Rodriguez-Gomez, V., Pillepich, A., Sales, L. V., et al. 2016, MNRAS, 458, 2371
Stinson, G. S., Dalcanton, J. J., Quinn, T., et al. 2009, MNRAS, 395, 1455
Tanaka, M., Chiba, M., Komiyama, Y., Guhathakurta, P., & Kalirai, J. S. 2011, ApJ, 738, 150
Tissera, P. B., Beers, T. C., Carollo, D., & Scannapieco, C. 2014, MNRAS, 439, 3128
Valcke, S., de Rijcke, S., & Dejonghe, H. 2008, MNRAS, 389, 1111